AAAS
Ultrafast Science
Volume 2022, Article ID 9760631, 12 pages
https://doi.org/10.34133/2022/9760631

Ultrafast Science
A SCIENCE PARTNER JOURNAL

Research Article

Birefringence-Managed Normal-Dispersion Fiber Laser Delivering Energy-Tunable Chirp-Free Solitons

Dong Mao,[1] Zhiwen He,[1] Qun Gao,[1] Chao Zeng,[1] Ling Yun,[2] Yueqing Du,[1] Hua Lu,[1] Zhipei Sun,[3] and Jianlin Zhao[1]

[1] *Northwestern Polytechnical University, School of Physical Science and Technology, Key Laboratory of Light Field Manipulation and Information Acquisition, Ministry of Industry and Information Technology, Shaanxi Key Laboratory of Optical Information Technology, Xi'an, China 710129*
[2] *Nanjing University of Posts and Telecommunications, College of Electronic and Optical Engineering & College of Microelectronics, Nanjing, China 210046*
[3] *Aalto University, Department of Electronics and Nanoengineering and QTF Centre of Excellence, Aalto, Finland*

Correspondence should be addressed to Zhipei Sun; zhipei.sun@aalto.fi and Jianlin Zhao; jlzhao@nwpu.edu.cn

Dong Mao and Zhiwen He contributed equally to this work.

Received 10 March 2022; Accepted 1 July 2022; Published 30 July 2022

Chirp-free solitons have been mainly achieved with anomalous-dispersion fiber lasers by the balance of dispersive and nonlinear effects, and the single-pulse energy is constrained within a relatively small range. Here, we report a class of chirp-free pulse in normal-dispersion erbium-doped fiber lasers, termed birefringence-managed soliton, in which the birefringence-related phase-matching effect dominates the soliton evolution. Controllable harmonic mode locking from 5 order to 85 order is obtained at the same pump level of ~10 mW with soliton energy fully tunable beyond ten times, which indicates a new birefringence-related soliton energy law, which fundamentally differs from the conventional soliton energy theorem. The unique transformation behavior between birefringence-managed solitons and dissipative solitons is directly visualized via the single-shot spectroscopy. The results demonstrate a novel approach of engineering fiber birefringence to create energy-tunable chirp-free solitons in normal-dispersion regime and open new research directions in fields of optical solitons, ultrafast lasers, and their applications.

1. Introduction

Mode-locked fiber lasers are capable of producing ultrashort pulse trains, which have found widespread use in fundamental physics [1–4] and related applications ranging from communication, metrology, and micromachining to microscopy [5–9]. By managing the nonlinearity and dispersion of fiber lasers, chirp-free solitons, dispersion-managed solitons, giant-chirped self-similar pulses, and dissipative solitons (DSs) have been demonstrated in the past several decades. Conventional chirp-free solitons arise from a delicate balance between the self-phase modulation and anomalous dispersion in optical fibers, typically featuring the Sech^2 intensity profile with pairs of spectral sidebands [10, 11]. Due to the soliton area theorem [12], the single-pulse energy is constrained within a relatively small range. Dispersion-managed solitons [13], also known as stretched pulses, are formed in near-zero-dispersion regimes where the pulses are strongly stretched and compressed due to the varying dispersion setting along the cavity [14, 15]. Self-similar pulses are formed in normal-dispersion regimes, featuring a parabolic spectral and temporal profile [16] due to the self-similar amplification in fiber lasers [2, 17]. DSs initially refer to confined wave packets of light formed in normal-dispersion regimes, where pulses experience the strong nonlinear gain and loss during propagation [18, 19]. On a theoretical view, the four types of pulses are solutions of the complex Ginzburg-Landau equation, in which static solution, breathing solution, asymptotic solution, and fixed localized solution correspond to conventional solitons,

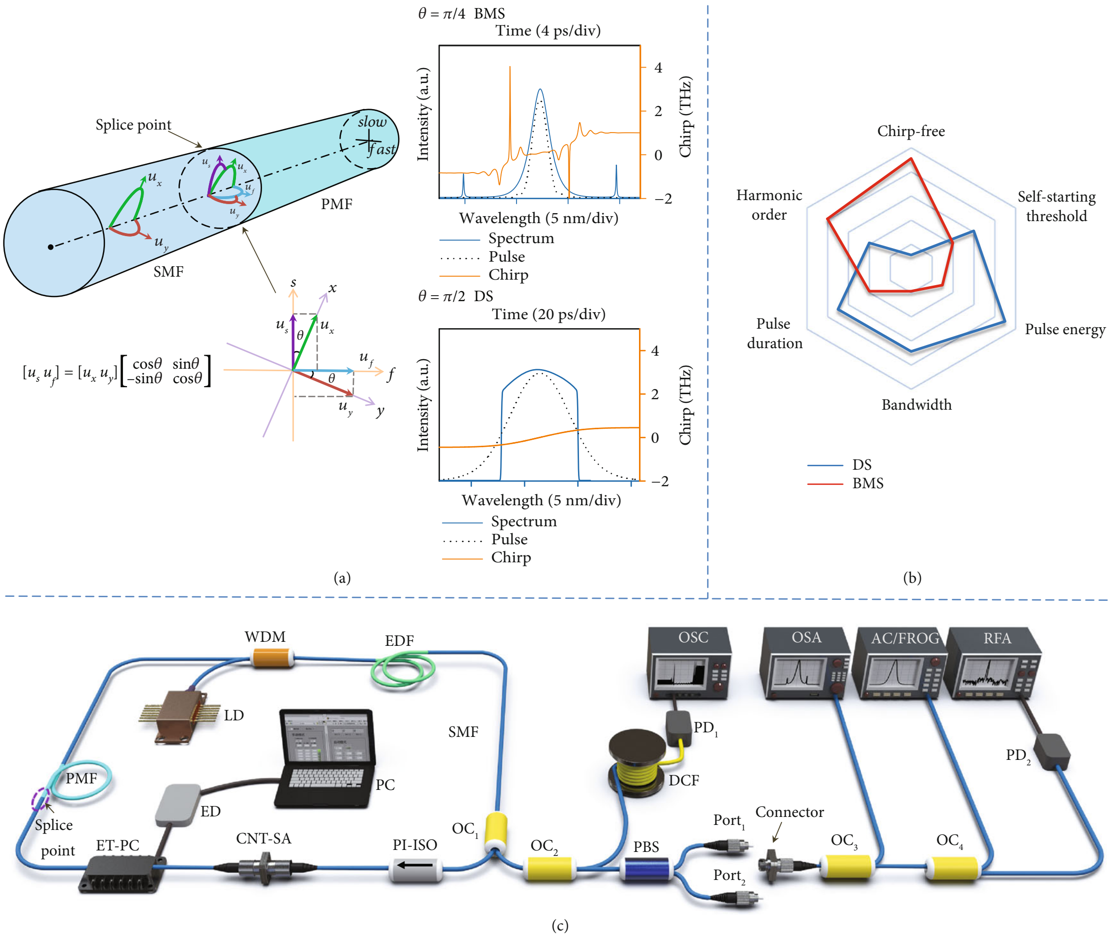

(a)

(b)

(c)

FIGURE 1: Concept and implementation of the birefringence-managed normal-dispersion fiber laser. (a) Coupling manner at the interface between SMF and PMF (left) and laser operations at different polarization orientations (right). The u_s and u_f components of pulses along two principal axes of PMF rely on the input polarization orientation θ as well as u_x and u_y components in SMF, following the relation depicted in the coordinate system. When $\theta = \pi/2$ or 0 (bottom right) and $\pi/4$ (top right), DS and BMS operations are achieved, respectively, in which the spectrum and chirp (pulse) are denoted by a solid (dot) curve. (b) Comparison of BMS and DS in the same fiber laser from aspects of frequency chirp, harmonic order, pulse duration, bandwidth, pulse energy, and self-starting threshold. (c) Sketch of the BMS fiber laser and measurement system. LD: laser diode; WDM: wavelength division multiplexer; EDF: erbium-doped fiber; OC: optical coupler; PI-ISO: polarization insensitive isolator; CNT-SA: carbon nanotube saturable absorber; ET-PC: electrically tunable polarization controller; ED: ET-PC driver; PC: personal computer; DCF: dispersion compensating fiber; PD: photodetector; PBS: polarizing beam splitter; OSA: optical spectrum analyzer; OSC: oscilloscope; AC: autocorrelator; FROG: frequency-resolved optical gating; RFA: radio frequency analyzer.

dispersion-managed solitons, self-similar pulses, and DSs, respectively [2, 16, 19]. These important advances mainly focused on the dispersion and nonlinear management of cavity and have certainly provided a profound insight into the understanding of soliton dynamics for numerous technological innovations. Nevertheless, exploring new types of solitons remains a fascinating subject in the context of mathematics and physics.

As a matter of fact, fiber birefringence is another key factor that affects the formation of solitons [20–23], e.g., highly stable scalar solitons in polarization-maintaining fiber (PMF) lasers [24, 25], group-velocity-locked vector solitons [26], and polarization-locked vector solitons [27] in low-birefringent fiber lasers. Compared with solitons formed in low-birefringent fiber lasers or all-PMF lasers, besides the chromatic dispersion and nonlinear effect, the fiber birefringence and polarization orientation of pulses should be considered particularly in hybrid-structure fiber lasers comprising single-mode fibers (SMFs) and PMFs [28], which however have received less attention. As such, the very attractive topics that naturally arise are to explore new types of solitons in hybrid-structure resonators and unveil their unique properties as well as formation mechanisms.

In this article, we numerically and experimentally demonstrate chirp-free solitons formed in normal-dispersion erbium-doped fiber (EDF) lasers by managing the cavity birefringence with a section of PMF (left panel of Figure 1(a)). Akin to that of the dispersion-managed soliton, we term it as birefringence-managed soliton (BMS) since the phase-matching effect dominated by the high-birefringent PMF greatly contributes to the formation of soliton. Compared with previously reported giant-chirped DSs [18, 19, 29, 30] or the DS emitted from the same cavity via changing the polarization orientation (e.g., θ is ~0 or $\sim\pi/2$, bottom-right panel of Figure 1(a)), the chirp-free BMSs (e.g., θ spans from $\sim\pi/10$ to $\sim 2\pi/5$, top-right panel of Figure 1(a)) have smaller pulse duration, bandwidth, and pulse energy, as well as self-starting threshold, and are capable of assembling themselves into high-order harmonic mode-locking states (tunable from 5 order to 85 order) at a comparatively small pump power of ~10 mW (Figure 1(b)). The single-pulse energy is fully tunable beyond ten times, indicating a new birefringence-related soliton energy law that fundamentally differs from the conventional soliton energy theorem [12]. These results provide an in-depth insight on the formation of BMS and open a way for directly generating energy-tunable femtosecond or picosecond pulses in normal-dispersion fiber lasers.

2. Materials and Methods

2.1. Experiment Setup. The fiber laser displayed in Figure 1(c) has a ring configuration comprising a wavelength division multiplexer (WDM), 15.3 m EDF (EDFC-980-HP), a 50 : 50 optical coupler (OC), a filmy carbon nanotube saturable absorber (CNT-SA), and 1 m PMF (PM1550-HP), as well as a polarization insensitive isolator (PI-ISO). The CNT-SA in the cavity is responsible for starting and maintaining the mode-locking operation. The PMF is employed to manage the birefringence of the cavity, which is indispensable for the formation of the BMS. The self-started mode-locking state can be realized and maintained once the pump strength reaches the threshold value. The two orthogonally polarized components along two principal axes of PMF depend on the input polarization direction in SMF that can be adjusted by the electrically tunable polarization controller (ET-PC), which results in reversible transition between BMS and DS mode-locking states. The pigtails of these fiber devices are SMFs (SMF-28e+) with a total length of 9.3 m. The dispersion parameters D for EDF, SMF, and PMF are given as -16.5, 17, and 17 ps (nm·km)$^{-1}$, respectively, giving the net cavity dispersion of ~0.1 ps^2. The beat lengths of PMF and other fibers are about 3.1 mm and 1 m, respectively.

The optical spectrum, duration, phase, and signal-to-noise ratio of the pulse are measured by an optical spectrum analyzer (OSA: Yokogawa, AQ6370), an autocorrelator (Pulsecheck, USB-150), a frequency-resolved optical gating (Femto Easy, FS-600), and a radio frequency analyzer (Agilent, E4440A), respectively. Except for the frequency-resolved optical gating measurement, the optical spectra, pulse trains, autocorrelation traces, and radio frequency spectra are directly measured without amplification. The real-time spectral dynamics are visualized by the dispersive Fourier transformation (DFT) system comprising a 2 km long dispersion-compensating fiber (DCF: YOFC, G652 DCF-C) with the dispersion of -150 ps (nm·km)$^{-1}$and a 5 GHz photodetector (THORLABS, DET09CFC/M) together with a 4 GHz real-time oscilloscope (LeCroy, 740Zi-A). The total accumulated dispersion after propagation through the DCF is 387 ps^2. According to the overall limitation of DFT on the spectral resolution [31], the electronic-based system possesses a spectral resolution of ~0.83 nm. It is worth noting that the length of DCF should be appropriately selected to simultaneously satisfy the far-field condition of the DFT method and distinguish each waveform of multiple BMSs without overlapping.

2.2. Simulation Model. We first simulate the formation and evolution of pulses that involve two orthogonally polarized components in the proposed fiber laser based on the lumped propagation model [32], in which each component of the cavity is modeled by a transmission function following the order shown in Figure 1(c) in a single roundtrip. Different from previous simulations, the coupling manner of pulse from SMF to PMF is specially considered in our model. As shown in Figure 1(a), the slightly birefringent SMF supports x-polarized (u_x) component and y-polarized (u_y) component of light. When the $u_x\ (u_y)$ component is launched with its polarization direction oriented at an angle of θ with respect to slow (fast) axis of the PMF, two orthogonally polarized components along the slow axis (u_s) and fast axis (u_f) of the PMF can be expressed with u_x and u_y following the relation described in Equation (1) [28]. After the PMF, the pulse propagates into the next section of SMF and the orientation angle is set as zero; thus, the $u_\mathrm{s}\ (u_\mathrm{f})$ component in PMF evolves to $u_x\ (u_y)$ component according to the following equation:

$$\left[u_\mathrm{s}\, u_\mathrm{f}\right] = \left[u_x\, u_y\right] \begin{bmatrix} \cos\theta & \sin\theta \\ -\sin\theta & \cos\theta \end{bmatrix} \tag{1}$$

The propagation of pulse involving two orthogonally polarized components in the SMF, EDF, and PMF is described by a pair of coupled Ginzburg-Landau equations [33] that include Kerr nonlinearity, dispersion, gain, and loss, as well as birefringence of each fiber:

$$\begin{aligned} \frac{\partial u_x}{\partial z} &= -i\beta u + \delta \frac{\partial u_x}{\partial t} - i\frac{\beta_2}{2}\frac{\partial^2 u_x}{\partial t^2} + i\gamma\left(\left|u_x\right|^2 + \frac{2}{3}\left|u_y\right|^2\right)u_x \\ &\quad + \frac{i\gamma {u_y}^2 {u_x}^*}{3} + \frac{(g-\alpha)}{2}u_x + \frac{g}{2\Omega_\mathrm{g}^2}\frac{\partial^2 u_x}{\partial t^2}, \\ \frac{\partial u_y}{\partial z} &= i\beta u_y - \delta \frac{\partial u_y}{\partial t} - i\frac{\beta_2}{2}\frac{\partial^2 u_y}{\partial t^2} + i\gamma\left(\left|u_y\right|^2 + \frac{2}{3}\left|u_x\right|^2\right)u_y \\ &\quad + \frac{i\gamma {u_x}^2 {u_y}^*}{3} + \frac{(g-\alpha)}{2}u_y + \frac{g}{2\Omega_\mathrm{g}^2}\frac{\partial^2 u_y}{\partial t^2}. \end{aligned} \tag{2}$$

The typical split-step Fourier technique is utilized to solve these coupled Ginzburg-Landau equations [32]. The variables u_x and u_y describe envelopes of each orthogonally polarized component. z corresponds to the cavity position while t relates to the time. Δn, $2\beta = 2\pi\Delta n/\lambda$, and $2\delta = 2\beta\lambda/2\pi c$ are refractive index difference, wave-number difference, and inverse group velocity difference of two orthogonally

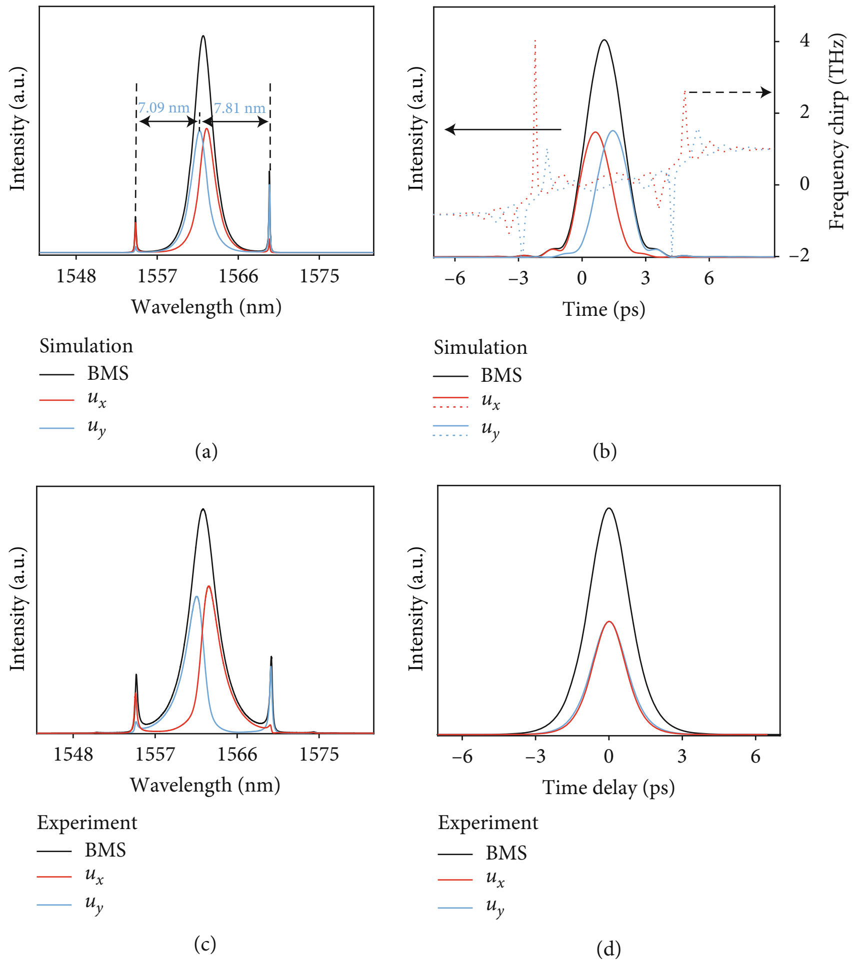

Figure 2: BMSs formed in an erbium-doped fiber laser. (a) Spectrum; (b) pulse profile and frequency chirp of simulated BMSs ($\theta = \pi/4$); (c) spectrum and (d) autocorrelation trace of measured BMSs.

polarized components, respectively. c is the speed of light in vacuum, λ is the peak wavelength, γ is cubic refractive nonlinearity, β_2 represents second-order dispersion coefficient, and α denotes the transmission loss of the optical fiber. Ω_g determines the gain bandwidth, and $g = g_0 \exp(-E_p/E_s)$ denotes the saturable gain, in which E_s, E_p, and g_0 are the gain saturation energy, pulse energy, and small-signal gain coefficient, respectively. The CNT-SA is modeled by the transmission function $T = 0.43 - T_0/[1 + P_{(\tau)}/P_{sat}]$, in which P_{sat} is the saturation intensity, $P_{(\tau)}$ is the instantaneous pulse intensity, and T_0 is the modulation depth.

The following parameters are used to implement the simulation: $c = 3 \times 10^8\,\mathrm{m\,s^{-1}}$, $\lambda = 1560\,\mathrm{nm}$, $\alpha = 4.6 \times 10^{-5}\,\mathrm{m^{-1}}$, $T_0 = 0.08$, and $P_{sat} = 11\,\mathrm{W}$. The SMF has a total length of 9.3 m with $\Delta n = 1.5 \times 10^{-6}$, $g_0 = 0$, $\gamma = 1.3 \times 10^{-3}\,\mathrm{W^{-1}\,m^{-1}}$, and $\beta_2 = -0.0219\,\mathrm{ps^2\,m^{-1}}$. For PMF, $\Delta n = 4.98 \times 10^{-4}$, $\gamma = 1.3 \times 10^{-3}\,\mathrm{W^{-1}\,m^{-1}}$, and the other parameters are the same as those of the SMF. For the 15.3 m EDF, $\Delta n = 1.5 \times 10^{-6}$, $g_0 = 0.7\,\mathrm{m^{-1}}$, $\gamma = 4.2 \times 10^{-3}\,\mathrm{W^{-1}\,m^{-1}}$, and $\beta_2 = 0.0213\,\mathrm{ps^2\,m^{-1}}$. The saturation energy is related to pump strength, which is set as 16.8 pJ for BMSs and 82 pJ for DSs.

3. Results and Discussion

3.1. Simulation and Experiment Results of Birefringence-Managed Solitons. The simulation starts from a same weak signal, and the final state of the laser mainly depends on θ. For example, in the range of 0 to $\pi/2$, giant-chirped DSs are formed when θ is ~0 or ~$\pi/2$ (see Supplementary Figure S1), while chirp-free BMSs are always obtained when θ varies between $\sim\pi/10$ and $\sim 2\pi/5$. Besides, when the θ ranges from 0 to $\sim\pi/10$ and $\sim 2\pi/5$ to $\sim\pi/2$, stable BMS mode locking cannot be realized in the fiber laser. Figures 2(a) and 2(b) display the typical simulation result of BMSs for θ of $\pi/4$ and PMF length of 1 m. The simulated spectrum displays a quasi-Sech^2 profile on a linear scale, which is somewhat similar to that of conventional solitons previously observed in the anomalous-dispersion regime [12]. Two sharp sidebands are clearly observed on the spectrum, and more spectral sidebands can be observed on a logarithmic scale (see Supplementary Figure S2). The u_x and u_y components of simulated BMSs have equivalent spectral intensities but with mirrored profiles. Taking u_y component (blue curve in Figure 2(a)) as an example, the two sidebands have different intensities, and the stronger sideband at longer wavelength is farther to its peak wavelength (~7.81 nm) than that of the weaker one at shorter wavelength (~7.09 nm). Evidently, the BMSs differ from group-velocity-locked vector solitons achieved in anomalous-dispersion fiber cavities, whose two orthogonally polarized components usually possess quasisymmetric spectral profiles with slightly different central wavelengths and sideband positions [10, 34].

The simulation results are fully corroborated by experiment observations via tuning the ET-PC before the PMF. Figures 2(c) and 2(d) display the spectra and autocorrelation traces of BMS and its two components. The pulse retrieved from frequency-resolved optical gating trace in Supplementary Figure S3 exhibits a flat phase over the central part of each component, which coincides with the simulated frequency chirp in Figure 2(b). The pulse duration and spectral bandwidth of BMSs in the simulation (experiment) are ~1.74 ps (~1.22 ps) and~2.42 nm (~3.42 nm) separately. Though the spectral bandwidth and pulse duration are slightly different for simulation and experiment, the time-bandwidth product of the simulated BMS is ~0.518, which agrees well with the experimental result (~0.513) and confirms the near-chirp-free property of BMSs. The slight difference arises from the incompletely determined parameters, such as the birefringence induced by the ET-PC. Besides, the small deviation from a transform-limited pulse is mainly resulted from the temporal and spectral separations of two components that result in a larger duration and bandwidth of BMSs. For each component, the time-bandwidth product is ~0.32.

3.2. Intracavity Evolution of BMSs. The dynamic evolution of BMSs and two orthogonally polarized components inside the EDF laser is studied to unveil the formation mechanism of the pulses. Figure 3(a) illustrates the position of fiber devices and the fiber dispersion parameters in the cavity, where the WDM is set as the starting point for a clear representation. Figure 3(b) shows the temporal evolution of two orthogonally polarized components (upper panel) and the total pulse (lower panel) along the cavity position, while Figure 3(c) corresponds to their spectral evolutions. In each roundtrip, two orthogonally polarized components of BMSs first pass through 1.1 m SMF and then enter the 15.3 m EDF. Influenced by the saturable amplification property of the gain medium, their intensities almost increase linearly in the forepart while they enlarge slowly in the rear part. Subsequently, two orthogonally polarized components are slightly compressed during propagating through 1.2 m SMF and extracted by the 50 : 50 coupler. After that, they are sharpened by the CNT-SA and the intensities decrease accordingly due to the nonsaturable loss of the saturable absorber.

At the cavity position of 23.6 m, the two orthogonally polarized components enter the PMF, as depicted in Figure 3(d). As demonstrated by Equation (1), when $\theta = \pi/4$, the u_y and u_x components couple equally to u_f and u_s components along fast and slow axes of PMF. Due to the high birefringence of PMF, u_s and u_f components move toward each other and collide near the central position of the PMF (~24.1 m). The duration of the total pulse depicted in Figure 3(e) decreases abruptly while the peak power increases suddenly in the colliding point. After that, two orthogonally polarized components separate from each other during propagation through the rest part of PMF. At the end of PMF, u_s and u_f components separately couple to u_x and u_y components in SMF for the next circulation. Actually, the birefringence of PMF and the orientation angle must be confined to a certain range for generating such BMSs. First, the total birefringence should be moderate to effectively control the spectral bandwidth while ensuring an appropriate separation between two components. Second, the energy proportion between u_x and u_y in u_s or u_f component should be close (i.e., θ ranges from $\sim\pi/10$ to $\sim 2\pi/5$) so that two pulses at fast and slow axes propagate in an "X" behavior in the PMF to realize self-consistent evolution.

We further analyze the intracavity evolution of key pulse parameters to ascertain the determining factor for pulse formation. The spectral bandwidth of BMS and its two components in Figure 4(a) changes slightly throughout the cavity, indicating that the intensity-related self-phase modulation effect is relatively small. For both u_x and u_y components, the spectral broadening is compensated by the mode coupling between them. In Figure 4(b), the duration of each component first decreases and then increases nonlinearly in the normal-dispersion EDF, which mainly results from the phase-matching effect discussed later. In contrast, the pulse duration changes linearly in the anomalous-dispersion SMF. As the temporal and spectral separations between two components change along the cavity, the BMS and its components exhibit different evolution behaviors such as duration, bandwidth, and TBP. Noting that, before and after passing through the CNT-SA, the spectral bandwidth enlarges while the pulse duration diminishes in accordance with the Fourier transform principle, and the TBPs of BMS and its two components in Figure 4(c) almost keep unchanged. Besides, at some special cavity positions (e.g., ~4 m and 24 m), the TBP of each component is slightly lower than 0.315, indicating that it deviates from the Sech^2 intensity profiles.

The evolution of DS inside the same cavity is given in Supplementary Figure S4 for comparison with that of BMS. When θ is $\sim\pi/2$, two orthogonally polarized components of DS in SMF propagate to PMF, $u_\mathrm{s} = -u_y$ and $u_\mathrm{f} = u_x$, according to Equation (1). After propagation through the PMF, $u_x = u_\mathrm{s}$ and $u_y = u_\mathrm{f}$ when they enter the next section of SMF. It is evident that, in each roundtrip, u_x component changes to u_y while u_y changes to $-u_x$. The physical picture is that, in one roundtrip, the u_x and u_y components are along the fast and slow axes of PMF, while in the next roundtrip, the u_x and u_y components are along the slow and fast axes, respectively. As such, two orthogonally polarized components evolve back and the birefringence-related effects in PMF are counterbalanced after even roundtrips of circulations; thus, the fiber laser can be viewed as a standard normal-dispersion fiber laser, in which the formation of DSs is attributed to the joint effects of normal cavity dispersion, gain filtering, as well as saturable absorption. The output

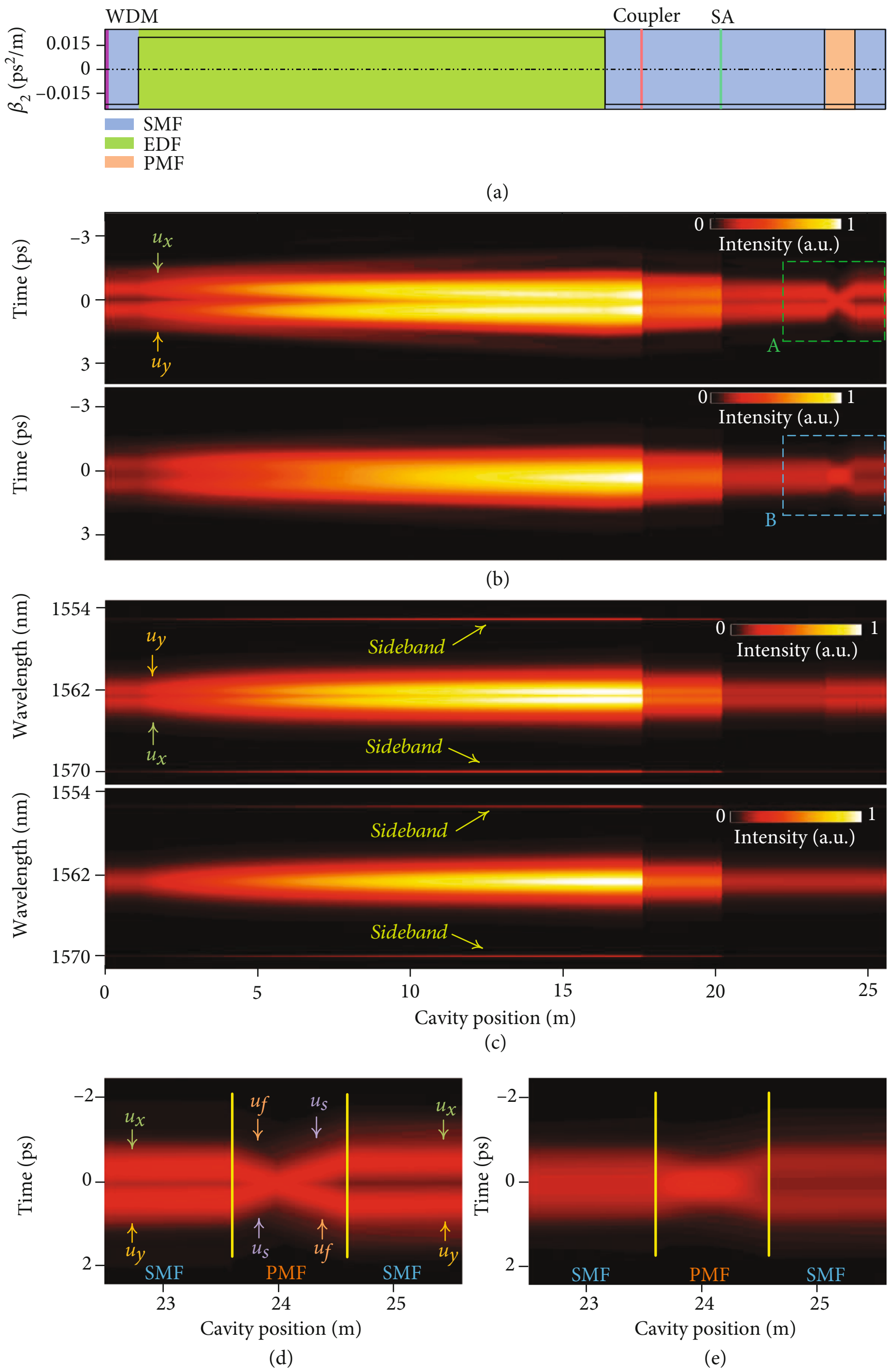

Figure 3: Evolution of BMSs inside the cavity. (a) Intracavity location of fiber devices and fiber dispersion parameters. (b) Temporal and (c) spectral evolutions of two components (upper panel) and BMSs (lower panel). (d, e) Close-ups of the A and B regions, respectively, elaborating the pulse evolution behaviors in the PMF region. The pulse and spectral intensities are normalized in color scale.

DSs exhibit similar behaviors as the previously observed DSs [25, 35–39], while they are markedly different from BMSs in aspects of spectral and temporal properties and formation mechanisms.

3.3. Formation Mechanism of BMSs. The formation mechanisms of BMSs and their spectral sidebands can be interpreted by the phase-matching principle that takes into account the fiber dispersion, birefringence, and nonlinear phase accumulated throughout the cavity. During transmission in the fiber resonator, the optical spectra of BMSs broaden due to the self-phase modulation effect. Conceptually similar to that of the conventional soliton [12, 40], two orthogonally polarized components of BMSs experience periodic perturbations in the resonator, such as gain and loss, as well as PMF-induced mode coupling, and they

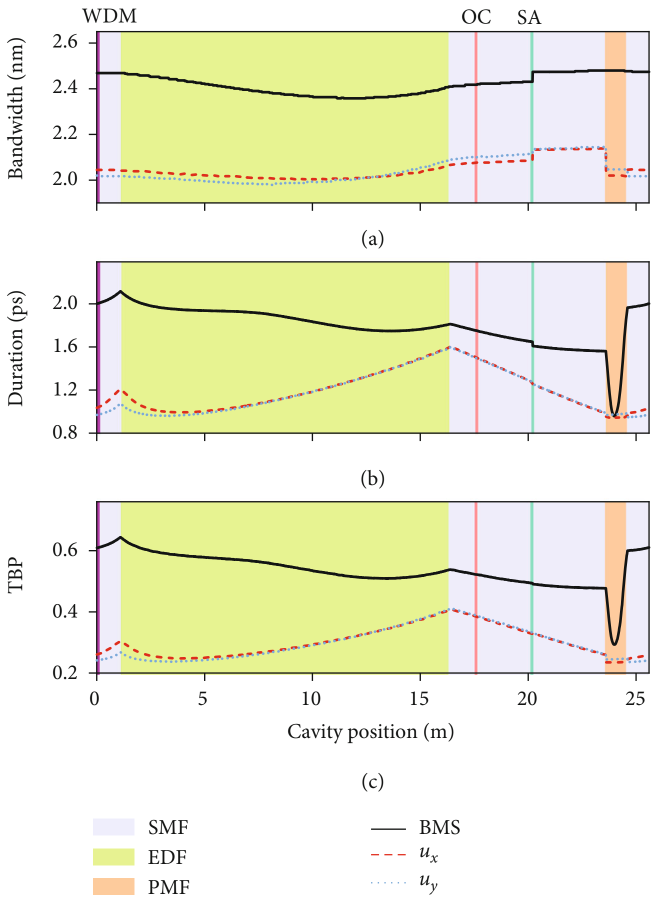

(a)

(b)

(c)

Figure 4: Evolution of key parameters along the cavity position for BMS and the two orthogonally polarized components: (a) bandwidth; (b) duration; (c) TBP.

emit new frequencies to realize the self-consistent evolution. These new-emerged frequencies (ω) are generated over the whole spectrum and propagate at different velocities with respect to the peak frequency (ω_0), which results in a phase difference that relies on the frequency offset ($\Delta\omega = \omega - \omega_0$). The detailed derivation of the phase difference has been elaborated in an all-normal-dispersion fiber laser [28]. For each roundtrip in the fiber laser, they can be expressed as

$$\begin{aligned} \Delta\varphi_x &= a\Delta\omega_x^2 - b\Delta\omega_x - \phi_{nlx}, \\ \Delta\varphi_y &= a\Delta\omega_y^2 + b\Delta\omega_y - \phi_{nly}, \\ a &= \frac{1}{2}\sum_i \beta_{2i} L_i, \\ b &= \frac{1}{2c}\sum_i \Delta n_i L_i. \end{aligned} \tag{3}$$

Here, $\Delta\omega_x$ and $\Delta\omega_y$ are frequency offsets between the peak frequency and sideband for u_x and u_y components of BMSs. $a\Delta\omega^2$, $b\Delta\omega$, and ϕ_{nl} account for the phase difference resulted from the chromatic dispersion, fiber birefringence, and nonlinear effects in a single roundtrip, respectively. β_{2i} represents the group velocity dispersion, and Δn_i denotes the refractive index difference between two orthogonally polarized components for each section of fiber with the length of L_i.

Such new-emerged frequencies generated in each period will interfere destructively except at frequencies that are phase-matched; i.e., $\Delta\varphi_{x/y}$ is 0 or the integer multiple of 2π. With the increase of frequency offset, the phase difference first enlarges from 0 to π, and the interference intensity changes from the maximum to minimum, which confines the spectra of BMSs and results in the quasi-Sech^2 spectral profile with a quite limited bandwidth. Remarkably, when the frequency offset reaches the value that satisfies the phase-matching relation expressed by Equation (4), the new-emerged frequencies will interfere constructively and form sharp spectral sidebands. The theoretical analysis explains the formation mechanism of BMS and the stronger sidebands of each orthogonally polarized component. Because u_x and u_y components are redistributed in PMF, a weaker sideband of u_x component always accompanies with the stronger sideband of u_y component at the same wavelength, and vice versa.

$$\begin{aligned} \Delta\omega_x &= \frac{b \pm \sqrt{b^2 + 4a(\phi_{nlx} + 2m\pi)}}{2a}, \\ \Delta\omega_y &= \frac{-b \pm \sqrt{b^2 + 4a\left(\phi_{nly} + 2m\pi\right)}}{2a}, \quad m = 1, 2, 3,. \cdots \end{aligned} \tag{4}$$

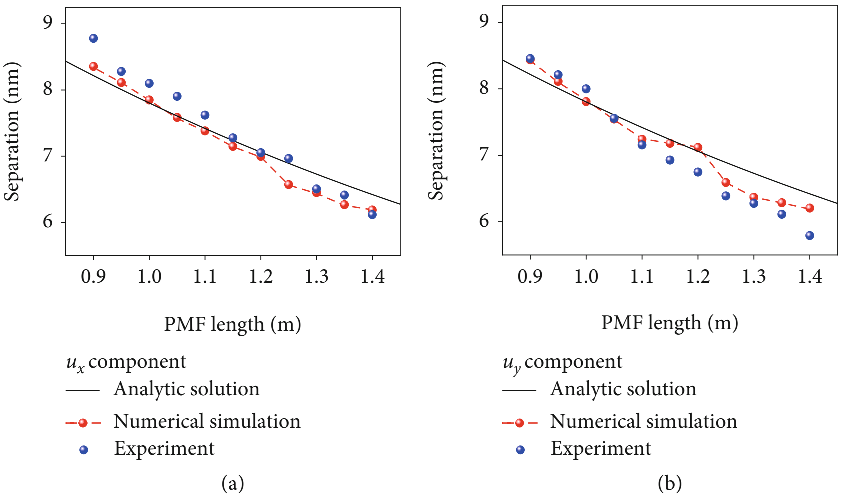

FIGURE 5: Spectral separation between the stronger sideband and peak wavelength of (a) u_x and (b) u_y components versus PMF length. The simulation results (dot line) and analytic solutions (solid line) are based on Equations (2) and (4), respectively.

Both simulation and experiment results show that BMSs can be formed when the PMF length of the proposed fiber laser ranges from 0.9 m to 1.4 m. We further compare the sideband separation of u_x and u_y components obtained from analytic predications based on Equation (4), numerical simulations via solving the Ginzburg-Landau equations, and experiment observations, as shown in Figures 5(a) and 5(b). All of them exhibit the similar evolution trend, which confirms the validity of numerical simulation and theoretical analysis and further validates the interpretation of the BMS formation as joint effects of strong birefringence, fiber nonlinearity, and normal dispersion. For each measurement, the ET-PC-induced birefringence and pulse power fluctuation are inevitable, resulting in the slight discrepancies among experimental, numerical, and theoretical results.

The formation mechanism of BMSs in normal-dispersion regime can be understood as follows. In the frequency domain, the spectrum of each BMS component broadens because of the fiber nonlinearity and emits new frequency due to periodic coupling at the input of PMF. However, it is confined in a narrow waveband with unique sidebands arising from the phase-matching effect. In the temporal domain, due to the limited bandwidth, the dispersion-induced stretching of pulses is weak and is easy to be counterbalanced by the saturable absorption effect. Thus, the combination of birefringence-related phase-matching effect, self-phase modulation, saturable absorption, and normal-dispersion enables the steady-state evolution in the dissipative system. As the formation depends on the coupling of two orthogonally polarized components, BMSs can only be achieved in fiber laser mode-locked by polarization-insensitive saturable absorbers.

3.4. Energy Tunability of BMSs. A fascinating phenomenon is that, besides the pump power, the number and pulse energy of BMSs per roundtrip strongly rely on the intracavity polarization conditions. For the state shown in Figures 2(c) and 2(d), five BMSs with an average power of 462 μW cocirculate inside the cavity under the pump of ~10 mW. By enhancing the pump strength alone, new BMS appears one by one from the cavity, which is similar to soliton splitting in the anomalous-dispersion regime [33]. Under the same pump power of ~10 mW, tunable harmonically mode-locked BMSs ranging from 5 order to 85 order are achieved by simply adjusting the ET-PC (Figure 6(a)), and the single-pulse energy is tunable beyond ten times (Figure 6(b)). The spectra, pulse trains, and radio frequency spectra of the typical harmonically mode-locked BMSs are given in Supplementary Figure S5.

Figures 6(c)–6(f) display pulse trains and radio frequency spectra of 5th and 85th harmonic mode-locking BMSs. Taking 85th harmonically mode-locked BMSs as an example, the pulses are equally distributed on the oscilloscope with a separation of 1.48 ns. The pulse has a repetition rate of 677.3 MHz, which is 85 times of cavity fundamental repetition rate (7.968 MHz). The signal-to-noise ratio exceeds 40 dB, validating the steadiness of harmonically mode-locked state. The formation mechanism of tunable harmonic mode locking can be understood as follows. As the polarization orientation angle θ relates to the perturbation of BMSs in the cavity [28], the pulse is less stable and prone to split into multiple pulses for a larger θ. Under the long-range repulsive interaction, the multiple pulses rearrange themselves into a uniform distribution and form harmonically mode-locked state.

A representative evolutionary process of harmonic mode locking is given in Movie S1, providing real-time view of harmonic mode-locking dynamics. Such operation intrinsically differs from previously reported harmonic mode locking that occurs at a relatively high pump level (usually hundreds of mW), which arises from the long-range repulsive interaction, and the repetition rate mainly relies on the pump power owing to the peak-power clamping effect [41–45]. This result confirms that the BMS follows a new birefringence-related soliton energy law with single-pulse energy tunable beyond ten times, indicating that the formation of BMS is less relevant with the pulse intensity, and it is fundamentally different from the conventional

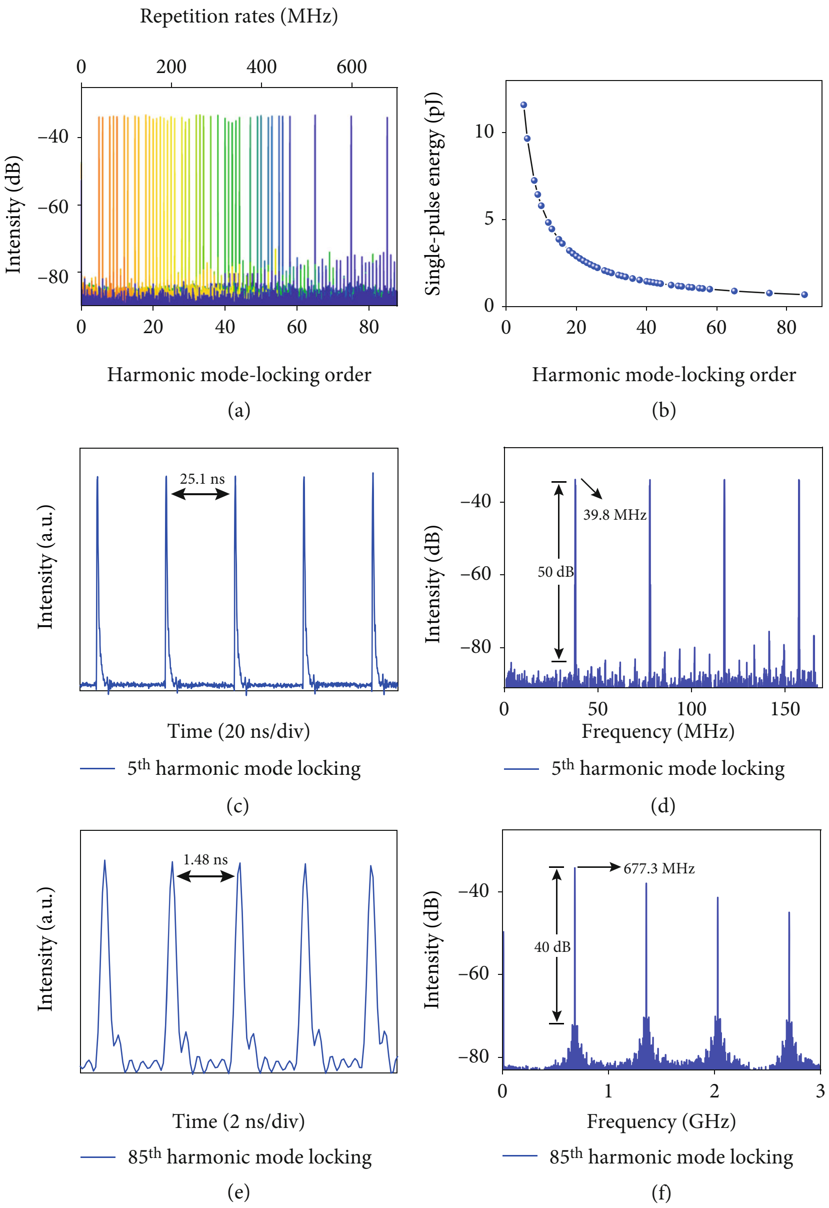

Figure 6: Energy tunability of BMSs. (a) Harmonic mode-locking order and repetition rate of BMSs realized via tuning the polarization state of light at pump power of ~10 mW. (b) Single-pulse energy versus different harmonic mode-locking orders. (c) Pulse trains and (d) radio frequency spectra of the 5th harmonic mode-locking BMSs. (e) Pulse trains and (f) radio frequency spectra of the 85th harmonic mode-locking BMSs.

soliton energy theorem that the single-pulse energy is constrained within a relatively small range [14]. Via enhancing the pump power to 12.4 mW, we obtain 117th harmonically mode-locked BMSs in the same fiber laser (see Supplementary Figure S6). However, the CNT-SA degenerates for pump power higher than 20 mW, which limits the available orders of harmonic mode locking. Harmonic mode locking up to several gigahertz may be achieved with a high-damage-threshold semiconductor saturable absorber.

3.5. Transient Transformation Behaviors between BMSs and DSs. To further corroborate normal-dispersion property of cavities, we record transformation processes between BMSs and DSs by a camera, as displayed in Movie S2. The transient dynamics of the transformation behavior in EDF laser are then studied using the single-shot spectroscopy based on DFT technique [31, 46–52]. The waveforms captured from the oscilloscope coincide with the time-averaged spectra measured by the OSA (see Supplementary Figure S7), confirming the validity of the measurement system. The time-continuous data stream is segmented according to the cavity roundtrip time, as shown in Figure 7, yielding a 2D graph where the x-axis depicts the roundtrip number, the y-axis represents roundtrip time, and the color denotes the spectral intensity of the pulse.

Figure 7(a) and Movie S3 show the transition process from BMSs to DSs, which lasts ~9100 roundtrips (~1.15 ms), and the concrete transition stages are outlined

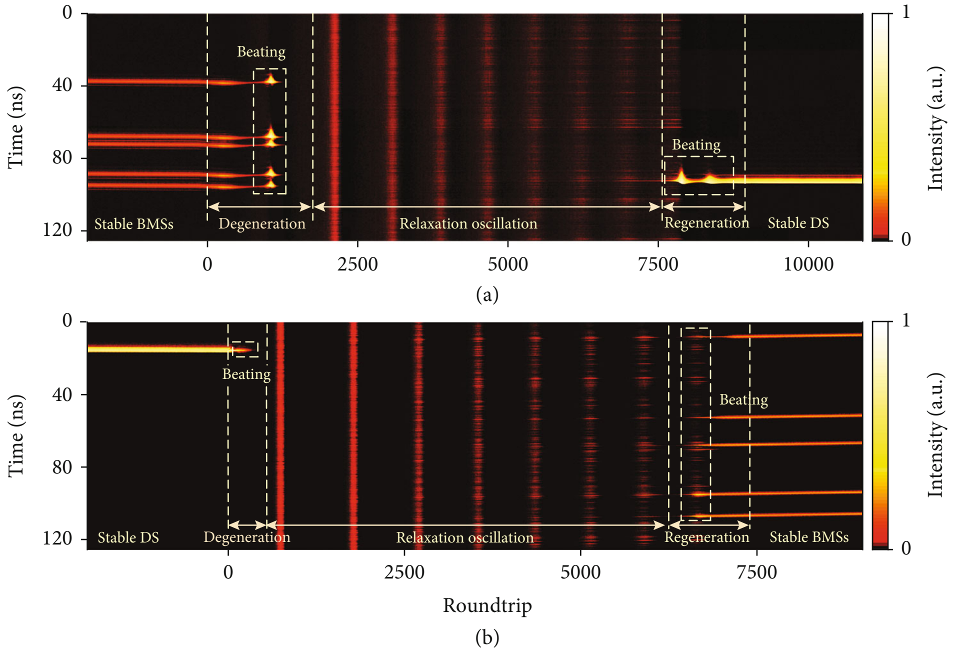

FIGURE 7: Transient switching behaviors between BMSs and DSs captured by the DFT technique with assistance of the ET-PC. (a) From BMSs to DSs and (b) from DSs to BMSs (intensity in color scale). The transition process includes the degeneration and beating of initial pulses, relaxation oscillation, beating, and regeneration of new pulses.

as follows. The fiber laser initially delivers five robust BMSs, and these pulses decay synchronously after changing θ by the ET-PC (defined as zero roundtrip). Then, a beating behavior occurs, in which five strong pulses with broadened spectra appear at the same cavity position as that of BMSs formed previously. This process lasts ~200 roundtrips, and an evident relaxation oscillation with long- and varying-period pulse spikes is observed successively. In this stage, the duration of each pulse spike increases from ~180 to 400 roundtrips and the separation of neighboring spikes decreases from ~800 to 700 roundtrips. At last several spikes, several small pulses grow up gradually at the same roundtrip time, meaning that they are formed at the same cavity position, known as the memory characteristic [53]. Significantly, the positions of such emerging pulses have no correspondence with any initial BMSs. After the relaxation oscillation stage, two consecutive beating spikes arise at the ~7800 roundtrip with the total duration of ~1200 roundtrips, and the intensity and width of pulse damply oscillate and finally develop into a stable DS. The transformation process from DSs to BMSs depicted in Figure 7(b) and Movie S4 resembles the inversion process from BMSs to DSs. The aforementioned results not only verify that the normal-dispersion fiber laser can be switched with great ease between BMSs and DSs operations but also reveal that the switching is dominated by a series of physical processes as diverse as degeneration and beating of initial pulses, relaxation oscillation, beating, and regeneration of new pulses.

4. Conclusion

It is concluded that the BMS is the fifth class of mode-locked pulse that intrinsically distinct from previously reported conventional solitons, stretched pulses, self-similar pulses, or dissipative solitons. First, BMSs directly generated from the normal-dispersion fiber laser are chirp-free with unique spectral sidebands, which fundamentally differs from the giant-chirped DSs [18, 19] or self-similar pulses [2, 17]. Second, the dispersion-managed solitons achieved in near-zero-dispersion regime usually exhibit broadband and smooth spectral profiles [15, 54], while the BMSs display narrowband spectra with sharp sidebands. Third, the Kelly sidebands of solitons in anomalous-dispersion regime mainly rely on the cavity dispersion [12, 40]. However, the sidebands of BMSs mainly depend on the birefringence of PMF and normal-dispersion of cavity. Most importantly, the order of harmonically mode-locked BMS can be varied over a large range at a relatively low pump level, and the soliton energy is fully tunable beyond ten times, also unlike that of other pulses primarily resting with the pump strength due to the soliton energy quantization effect [33].

Apart from chromatic dispersion, nonlinearity, and saturable absorption effects, we show that the birefringence of PMF can be exploited to manage the spectrum and the duration of pulse in the normal-dispersion regime, which opens new research directions in fields of optical solitons and ultrafast lasers. From an application perspective, this work paves an avenue to generate chirp-free ultrashort pulses in normal-dispersion EDF laser without external recompression, particularly appealing for the waveband lacking anomalous-dispersion fibers such as ytterbium-doped fiber lasers [38] and visible fiber lasers [55]. Such flexible fiber lasers are capable of producing high-order harmonically mode-locked BMSs with pulse energy tunable beyond ten times, also providing a promising way for realizing high-repetition-rate pulse sources with low power consumption for optical communication and sensing [56].

Data Availability

The data that support the plots within this paper and other findings of this study are available from the corresponding authors upon reasonable request.

Conflicts of Interest

The authors declare that there is no conflict of interest regarding the publication of this article.

Authors' Contributions

D. Mao designed the experiment, carried out the simulation as well as theoretical analysis, and wrote the manuscript. Z. He performed the experiments with the assistance of Q. Gao and L. Yun. C. Zeng, Y. Du, and H. Lu plotted the figures and discussed the results. Z. Sun and J. Zhao contributed to the interpreting of the results and revising of the manuscript. Dong Mao and Zhiwen He contributed equally to this work.

Acknowledgments

This work was supported by the National Key R&D Program of China (2017YFA0303800), National Natural Science Foundation of China (11874300, 61805277), the Fundamental Research Funds for the Central Universities (3102019JC008), and the Natural Science Foundation of Shaanxi Province (2021JC-09, 2019JQ-447).

Supplementary Materials

Figure S1: simulation and experiment results of DSs formed in the same fiber laser. Figure S2: fitting results and logarithmic spectra of BMSs. Figure S3: retrieved frequency-resolved optical gating traces of BMSs and two components. Figure S4: intracavity temporal and spectral evolution of DSs. Figure S5: five typical harmonically mode-locked BMSs at the pump power of 10.2 mW. Figure S6: 117th harmonically mode-locked BMSs achieved at the pump power of 12.4 mW. Figure S7: validity of DFT technique. Movie S1: real-time harmonic mode-locking dynamics of BMS. Movie S2: transformation processes between BMSs and DSs recorded by a camera. Movie S3: real time revealing the transition process from BMSs to DSs. Movie S4: real time revealing the transition process from DSs to BMSs. *(Supplementary Materials)*

References

[1] M. Peccianti, A. Pasquazi, Y. Park et al., "Demonstration of a stable ultrafast laser based on a nonlinear microcavity," *Nature Communications*, vol. 3, no. 1, p. 765, 2012.

[2] J. M. Dudley, C. Finot, D. J. Richardson, and G. Millot, "Self-similarity in ultrafast nonlinear optics," *Nature Physics*, vol. 3, no. 9, pp. 597–603, 2007.

[3] C. Lecaplain, P. Grelu, J. M. Soto-Crespo, and N. Akhmediev, "Dissipative rogue waves generated by chaotic pulse bunching in a mode-locked laser," *Physical Review Letters*, vol. 108, no. 23, article 233901, 2012.

[4] U. Keller, "Recent developments in compact ultrafast lasers," *Nature*, vol. 424, no. 6950, pp. 831–838, 2003.

[5] X. Yuan, T. Yang, J. Chen et al., "Experimental observation of vector solitons in a highly birefringent cavity of ytterbium-doped fiber laser," *Optics Express*, vol. 21, no. 20, pp. 23866–23872, 2013.

[6] M. E. Fermann and I. Hartl, "Ultrafast fibre lasers," *Nature Photonics*, vol. 7, no. 11, pp. 868–874, 2013.

[7] D. G. Abdelsalam Ibrahim and T. Yasui, "High-precision 3D surface topography measurement using high-stable multi-wavelength digital holography referenced by an optical frequency comb," *Optics Letters*, vol. 43, no. 8, pp. 1758–1761, 2018.

[8] M. Ebrahim-Zadeh and S. Chaitanya Kumar, "Yb-fiber-laser-pumped ultrafast frequency conversion sources from the mid-infrared to the ultraviolet," *IEEE Journal of Selected Topics in Quantum Electronics*, vol. 20, no. 5, pp. 624–642, 2014.

[9] Z. Lin and M. Hong, "Femtosecond laser precision engineering: from micron, submicron, to nanoscale," *Ultrafast Science*, vol. 2021, article 9783514, 22 pages, 2021.

[10] D. Y. Tang, H. Zhang, L. M. Zhao, and X. Wu, "Observation of high-order polarization-locked vector solitons in a fiber laser," *Physical Review Letters*, vol. 101, no. 15, article 153904, 2008.

[11] D. Brida, G. Krauss, A. Sell, and A. Leitenstorfer, "Ultrabroadband Er:fiber lasers," *Laser & Photonics Reviews*, vol. 8, no. 3, pp. 409–428, 2014.

[12] L. E. Nelson, D. J. Jones, K. Tamura, H. A. Haus, and E. P. Ippen, "Ultrashort-pulse fiber ring lasers," *Applied Physics B: Lasers and Optics*, vol. 65, no. 2, pp. 277–294, 1997.

[13] K. Tamura, E. P. Ippen, H. A. Haus, and L. E. Nelson, "77-fs pulse generation from a stretched-pulse mode-locked all-fiber ring laser," *Optics Letters*, vol. 18, no. 13, pp. 1080–1082, 1993.

[14] S. K. Turitsyn, B. G. Bale, and M. P. Fedoruk, "Dispersion-managed solitons in fibre systems and lasers," *Physics Reports*, vol. 521, no. 4, pp. 135–203, 2012.

[15] W. He, M. Pang, C. R. Menyuk, and P. St. J. Russell, "Sub-100-fs 187 GHz mode-locked fiber laser using stretched-soliton effects," *Optica*, vol. 3, no. 12, pp. 1366–1372, 2016.

[16] F. Ö. Ilday, J. R. Buckley, W. G. Clark, and F. W. Wise, "Self-Similar evolution of parabolic pulses in a laser," *Physical Review Letters*, vol. 92, no. 21, article 213902, 2004.

[17] B. Oktem, C. Ülgüdür, and F. Ö. Ilday, "Soliton-similariton fibre laser," *Nature Photonics*, vol. 4, no. 5, pp. 307–311, 2010.

[18] K. Kieu, W. H. Renninger, A. Chong, and F. W. Wise, "Sub-100 fs pulses at watt-level powers from a dissipative-soliton fiber laser," *Optics Letters*, vol. 34, no. 5, pp. 593–595, 2009.

[19] P. Grelu and N. Akhmediev, "Dissipative solitons for mode-locked lasers," *Nature Photonics*, vol. 6, no. 2, pp. 84–92, 2012.

[20] J. W. Haus, G. Shaulov, E. A. Kuzin, and J. Sanchez-Mondragon, "Vector soliton fiber lasers," *Optics Letters*, vol. 24, no. 6, pp. 376–378, 1999.

[21] B. C. Collings, S. T. Cundiff, N. N. Akhmediev, J. M. Soto-Crespo, K. Bergman, and W. H. Knox, "Polarization-locked temporal vector solitons in a fiber laser: experiment," *Journal of the Optical Society of America B*, vol. 17, no. 3, pp. 354–365, 2000.

[22] Y. S. Fedotov, S. M. Kobtsev, R. N. Arif, A. G. Rozhin, C. Mou, and S. K. Turitsyn, “Spectrum-, pulsewidth-, and wavelength-switchable all-fiber mode-locked Yb laser with fiber based birefringent filter,” *Optics Express*, vol. 20, no. 16, pp. 17797–17805, 2012.

[23] S. V. Sergeyev, H. Kbashi, N. Tarasov, Y. Loiko, and S. A. Kolpakov, “Vector-resonance-multimode instability,” *Physical Review Letters*, vol. 118, no. 3, article 033904, 2017.

[24] D. J. Jones, H. A. Haus, and E. P. Ippen, “Subpicosecond solitons in an actively mode-locked fiber laser,” *Optics Letters*, vol. 21, no. 22, pp. 1818–1820, 1996.

[25] A. Chong, W. H. Renninger, and F. W. Wise, “Environmentally stable all-normal-dispersion femtosecond fiber laser,” *Optics Letters*, vol. 33, no. 10, pp. 1071–1073, 2008.

[26] M. N. Islam, C. D. Poole, and J. P. Gordon, “Soliton trapping in birefringent optical fibers,” *Optics Letters*, vol. 14, no. 18, pp. 1011–1013, 1989.

[27] S. T. Cundiff, B. C. Collings, N. N. Akhmediev, J. M. Soto-Crespo, K. Bergman, and W. H. Knox, “Observation of polarization-locked vector solitons in an optical fiber,” *Physical Review Letters*, vol. 82, no. 20, pp. 3988–3991, 1999.

[28] D. Mao, Z. He, Y. Zhang et al., “Phase-matching-induced near-chirp-free solitons in normal-dispersion fiber lasers,” *Light: Science & Applications*, vol. 11, no. 1, p. 25, 2022.

[29] H. Zhang, D. Tang, R. J. Knize, L. Zhao, Q. Bao, and K. P. Loh, “Graphene mode locked, wavelength-tunable, dissipative soliton fiber laser,” *Applied Physics Letters*, vol. 96, no. 11, article 111112, 2010.

[30] W. Tian, Z. Wang, J. Liu et al., “Dissipative soliton and synchronously dual-wavelength mode-locking Yb:YSO lasers,” *Optics Express*, vol. 23, no. 7, pp. 8731–8739, 2015.

[31] K. Goda and B. Jalali, “Dispersive Fourier transformation for fast continuous single-shot measurements,” *Nature Photonics*, vol. 7, no. 2, pp. 102–112, 2013.

[32] G. P. Agrawal, *Nonlinear Fiber Optics*, Academic Press, New York, 3th edition, 2001.

[33] D. Y. Tang, L. M. Zhao, B. Zhao, and A. Q. Liu, “Mechanism of multisoliton formation and soliton energy quantization in passively mode-locked fiber lasers,” *Physical Review A*, vol. 72, no. 4, article 043816, 2005.

[34] L. M. Zhao, D. Y. Tang, H. Zhang, X. Wu, and N. Xiang, “Soliton trapping in fiber lasers,” *Optics Express*, vol. 16, no. 13, pp. 9528–9533, 2008.

[35] H. Zhang, D. Y. Tang, L. M. Zhao, X. Wu, and H. Y. Tam, “Dissipative vector solitons in a dispersionmanaged cavity fiber laser with net positive cavity dispersion,” *Optics Express*, vol. 17, no. 2, pp. 455–460, 2009.

[36] S. A. Babin, E. V. Podivilov, D. S. Kharenko et al., “Multicolour nonlinearly bound chirped dissipative solitons,” *Nature Communications*, vol. 5, no. 1, article 4653, 2014.

[37] D. Mao, X. Liu, D. Han, and H. Lu, “Compact all-fiber laser delivering conventional and dissipative solitons,” *Optics Letters*, vol. 38, no. 16, pp. 3190–3193, 2013.

[38] F. W. Wise, A. Chong, and W. H. Renninger, “High-energy femtosecond fiber lasers based on pulse propagation at normal dispersion,” *Laser & Photonics Review*, vol. 2, no. 1-2, pp. 58–73, 2008.

[39] K. Ozgoren and F. Ö. Ilday, “All-fiber all-normal dispersion laser with a fiber-based Lyot filter,” *Optics Letters*, vol. 35, no. 8, pp. 1296–1298, 2010.

[40] S. M. J. Kelly, “Characteristic sideband instability of periodically amplified average soliton,” *Electronics Letters*, vol. 28, no. 8, pp. 806-807, 1992.

[41] A. B. Grudinin, D. J. Richardson, and D. N. Payne, “Passive harmonic modelocking of a fibre soliton ring laser,” *Electronics Letters*, vol. 29, no. 21, pp. 1860-1861, 1993.

[42] S. Gray, A. B. Grudinin, W. H. Loh, and D. N. Payne, “Femtosecond harmonically mode-locked fiber laser with time jitter below 1 ps,” *Optics Letters*, vol. 20, no. 2, pp. 189–191, 1995.

[43] G. Sobon, J. Sotor, and K. M. Abramski, “Passive harmonic mode-locking in Er-doped fiber laser based on graphene saturable absorber with repetition rates scalable to 2.22 GHz,” *Applied Physics Letters*, vol. 100, no. 16, article 161109, 2012.

[44] Q. Hao, Y. Wang, P. Luo, H. Hu, and H. Zeng, “Self-starting dropout-free harmonic mode-locked soliton fiber laser with a low timing jitter,” *Optics Letters*, vol. 42, no. 12, pp. 2330–2333, 2017.

[45] X. Wang, J. Peng, K. Huang, M. Yan, and H. Zeng, “Experimental study on buildup dynamics of a harmonic mode-locking soliton fiber laser,” *Optics Express*, vol. 27, no. 20, pp. 28808–28815, 2019.

[46] A. Mahjoubfar, D. V. Churkin, S. Barland, N. Broderick, S. K. Turitsyn, and B. Jalali, “Time stretch and its applications,” *Nature Photonics*, vol. 11, no. 6, pp. 341–351, 2017.

[47] G. Herink, F. Kurtz, B. Jalali, D. R. Solli, and C. Ropers, “Real-time spectral interferometry probes the internal dynamics of femtosecond soliton molecules,” *Science*, vol. 356, no. 6333, pp. 50–54, 2017.

[48] P. Ryczkowski, M. Närhi, C. Billet, J. M. Merolla, G. Genty, and J. M. Dudley, “Real-time full-field characterization of transient dissipative soliton dynamics in a mode-locked laser,” *Nature Photonics*, vol. 12, no. 4, pp. 221–227, 2018.

[49] Z. Q. Wang, K. Nithyanandan, A. Coillet, P. Tchofo-Dinda, and P. Grelu, “Optical soliton molecular complexes in a passively mode-locked fibre laser,” *Nature Communications*, vol. 10, no. 1, p. 830, 2019.

[50] J. Peng, S. Boscolo, Z. Zhao, and H. Zeng, “Breathing dissipative solitons in mode-locked fiber lasers,” *Science Advances*, vol. 5, no. 11, article eaax1110, 2019.

[51] G. Herink, B. Jalali, C. Ropers, and D. R. Solli, “Resolving the build-up of femtosecond mode-locking with single-shot spectroscopy at 90 MHz frame rate,” *Nature Photonics*, vol. 10, no. 5, pp. 321–326, 2016.

[52] Y. Wang, X. Wang, J. Peng, M. Yan, K. Huang, and H. Zeng, “Experimental observation of transient mode-locking in the build-up stage of a soliton fiber laser,” *Chinese Optics Letters*, vol. 19, no. 7, article 071401, 2021.

[53] X. Liu, X. Yao, and Y. Cui, “Real-time observation of the buildup of soliton molecules,” *Physical Review Letters*, vol. 121, no. 2, article 023905, 2018.

[54] X. Dong, Q. Yang, C. Spiess, V. G. Bucklew, and W. H. Renninger, “Stretched-pulse soliton Kerr resonators,” *Physical Review Letters*, vol. 125, no. 3, article 033902, 2020.

[55] J. Zou, C. Dong, H. Wang, T. du, and Z. Luo, “Towards visible-wavelength passively mode-locked lasers in all-fibre format,” *Light: Science & Applications*, vol. 9, no. 1, p. 61, 2020.

[56] H. A. Haus and W. S. Wong, “Solitons in optical communications,” *Reviews of Modern Physics*, vol. 68, no. 2, pp. 423–444, 1996.